

# Many-Body Quantum Muon Effects and Quadrupolar Coupling in Solids

Matjaž Gomilšek <sup>1,2,3,\*</sup>, Francis L. Pratt <sup>4</sup>, Stephen P. Cottrell <sup>4</sup>, Stewart J. Clark <sup>3</sup> and Tom Lancaster <sup>3</sup>

<sup>1</sup>Jožef Stefan Institute, Jamova c. 39, SI-1000 Ljubljana, Slovenia

<sup>2</sup>Faculty of Mathematics and Physics, University of Ljubljana, Jadranska u. 19, SI-1000 Ljubljana, Slovenia

<sup>3</sup>Department of Physics, Durham University, South Road, Durham DH1 3LE, United Kingdom

<sup>4</sup>ISIS Muon Group, Science and Technology Facilities Council (STFC), Didcot OX11 0QX, United Kingdom

(Dated: June 22, 2023)

Strong quantum zero-point motion (ZPM) of light nuclei and other particles is a crucial aspect of many state-of-the-art quantum materials. However, it has only recently begun to be explored from an *ab initio* perspective, through several competing approximations. Here we develop a unified description of muon and light nucleus ZPM and establish the regimes of anharmonicity and positional quantum entanglement where different approximation schemes apply. Via density functional theory and path-integral molecular dynamics simulations we demonstrate that in solid nitrogen,  $\alpha$ -N<sub>2</sub>, muon ZPM is both strongly anharmonic and many-body in character, with the muon forming an extended electric-dipole polaron around a central, quantum-entangled [N<sub>2</sub>- $\mu$ -N<sub>2</sub>]<sup>+</sup> complex. By combining this quantitative description of quantum muon ZPM with precision muon quadrupolar level-crossing resonance experiments, we independently determine the static <sup>14</sup>N nuclear quadrupolar coupling constant of pristine  $\alpha$ -N<sub>2</sub> to be  $-5.36(2)$  MHz, a significant improvement in accuracy over the previously-accepted value of  $-5.39(5)$  MHz, and a validation of our unified description of light-particle ZPM.

## INTRODUCTION

Quantum zero-point motion (ZPM) of nuclei plays a pivotal role in the structure and dynamics of many important classes of materials, especially those containing light atoms such as hydrogen or lithium<sup>1-3</sup>. Prominent examples of this include recent record high- $T_c$  hydride superconductors<sup>4-10</sup>, record-density hydrogen storage materials<sup>11</sup>, metallic and solvated Li and F<sup>12,13</sup>, as well as many hydrogen-bonded materials<sup>2</sup>, e.g., water ice. Outside nuclear quantum effects, ZPM should be even more pronounced for implanted muons  $\mu^+$ , which act as sensitive probes in muon spin relaxation ( $\mu$ SR) experiments<sup>14-16</sup>, since a muon has just 1/9 of the proton mass. We expect a large muon zero-point energy  $ZPE \propto m_\mu^{-1/2} \sim 0.7$  eV<sup>15,17-22</sup>, corresponding ZPM delocalization  $\Delta x \propto m_\mu^{-1/4} \sim 0.2$  Å around isolated muon stopping sites, the merging of candidate muon sites separated by low energy barriers, quantum tunneling, diffusion, and even muon Bloch waves<sup>23,24</sup>. Beyond these, many-body quantum effects like positional entanglement between muons and nuclei are also expected. Muon ZPM challenges the approach of predicting muon stopping sites and the lattice distortions around them using *ab initio* methods, often based on density functional theory (DFT)<sup>17-19,25</sup>, that treats the muon and nuclei as classical particles. Several schemes for approximating muon ZPM have been developed<sup>18,19</sup>, mainly divisible into: (i) adiabatic methods, based on a single-particle description<sup>22,26-29</sup>, and (ii) harmonic approximations<sup>20,30,31</sup>. Studies of quantum muons using computationally more demanding, but numerically-exact, path-integral molecular dynamics (PIMD) have remained

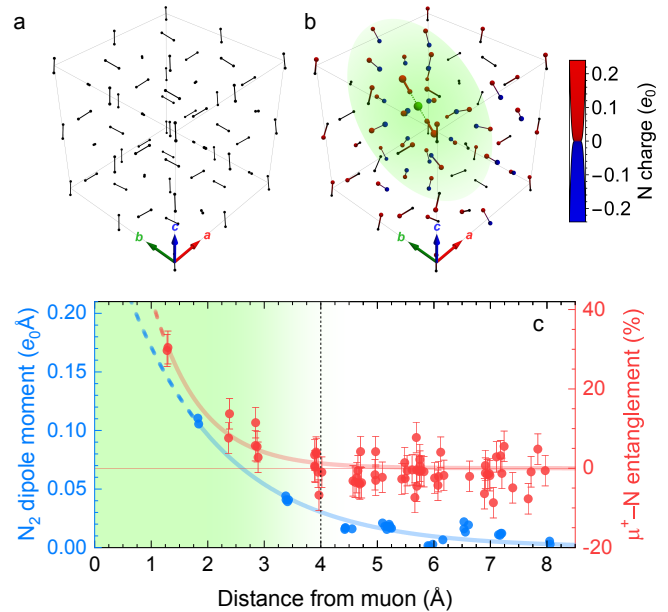


**Fig. 1. Muon site and muon–nuclear entanglement.** **a** Pristine  $\alpha$ -N<sub>2</sub> crystal structure in a  $2 \times 2 \times 2$  supercell. See also Supplementary Movie 1. **b** Classical muon  $\mu^+$  (green) in  $\alpha$ -N<sub>2</sub> induces an electric-dipole polaron (shading) around a linear [N<sub>2</sub>- $\mu$ -N<sub>2</sub>]<sup>+</sup> complex. Sphere size/color gives the induced Mulliken charge of nitrogen ions. See also Supplementary Movie 2. **c** Induced N<sub>2</sub> Mulliken electric dipole moments (blue) and degree of muon–nuclear positional entanglement  $c$  [Eq. (1)] from path-integral molecular dynamics (PIMD; red). Solid lines are exponential fits, dashed line/shading indicates the polaron size.  $c$  error bars represent a systematic uncertainty of one standard deviation (see Methods).

rather sparse<sup>1,24,32</sup>, despite its popularity in describing light-nuclei systems<sup>1-3</sup>.

\* Corresponding author. Email: [matjaz.gomilsek@ijs.si](mailto:matjaz.gomilsek@ijs.si)

Here we develop a unified description of muon and light nuclei ZPM and the regimes in which particular approximations apply, via a DFT+PIMD study of muon ZPM in solid nitrogen,  $\alpha$ -N<sub>2</sub> (Fig. 1a and Supplementary Fig. 1a). We characterize the regimes by the degree of (i) anharmonicity and (ii) muon–nuclear positional entanglement, the latter quantified with easy-to-calculate entanglement witnesses<sup>33–35</sup>. We find that in  $\alpha$ -N<sub>2</sub> anharmonic many-body quantum effects dominate, as anticipated from previous experimental<sup>23</sup> and theoretical work<sup>36</sup>, and discover that an extended electric-dipole polaron of polarized N<sub>2</sub> molecules forms around a central [N<sub>2</sub>– $\mu$ –N<sub>2</sub>]<sup>+</sup> complex (Fig. 1b). By applying these insights to our precision muon quadrupolar level-crossing resonance (QLCR)<sup>37–39</sup> experiments, we derive an independent estimate of the static nuclear quadrupolar coupling constant (NQCC) of <sup>14</sup>N with significantly improved accuracy compared to the literature value<sup>40</sup>.

## RESULTS

### Classical muon

Within the classical, point-particle description of muons and nuclei using DFT, we find a single stable muon site at almost exactly the (0, 1/4, 1/4) position (Fig. 1b and Supplementary Fig. 1b), which lies between two molecules of pristine  $\alpha$ -N<sub>2</sub> but is not symmetric under its  $Pa\bar{3}$  space group<sup>41,42</sup>. In line with *ab initio* simulations of muons<sup>36</sup> and protons<sup>43–47</sup> in N<sub>2</sub> clusters, we find that in crystalline  $\alpha$ -N<sub>2</sub> a muon forms an almost-linear, almost-centrosymmetric [N<sub>2</sub>– $\mu$ –N<sub>2</sub>]<sup>+</sup> complex oriented along the [0, 1, 1] direction. Within this complex the muon’s bare positive charge + $e_0$  is screened to just +0.46 $e_0$  by electrons covalently shared with the two nearest N<sub>2</sub> molecules, leaving them with an electron density deficit and thus a net positive charge of +0.27 $e_0$  each (+0.04 $e_0$  on the two nearest N atoms and +0.23 $e_0$  on the two further-away ones; Fig. 1b and Supplementary Fig. 2). Moreover, we find that an unusual, extended electric-dipole polaron forms around this complex, where its positive charge further induces electric dipole moments (Fig. 1c) on other, net neutral nearby N<sub>2</sub> molecules (Supplementary Fig. 2) and causes them to reorient to point towards the complex. Up to  $\sim 4$  Å from the muon, dipolar electrostatic interactions of polarized N<sub>2</sub> molecules with the [N<sub>2</sub>– $\mu$ –N<sub>2</sub>]<sup>+</sup> complex thus overwhelm the weak electric quadrupole and van der Waals (VdW) N<sub>2</sub>–N<sub>2</sub> interactions of pristine  $\alpha$ -N<sub>2</sub><sup>40,48</sup>.

### Single-particle quantum approximations

To incorporate quantum effects we first employ single-particle, adiabatic approximations of muon–nuclear ZPM. Though elaborate schemes have been proposed<sup>22,29</sup>, the simplest are weakly- and strongly-bound muon approximations<sup>26–28</sup>, corresponding to zero or maximal muon–nuclear entanglement, respectively. In both schemes, an effective single-particle muon potential  $V_{\text{eff}}(\delta\mathbf{x})$  is constructed from total DFT energy under muon displacements  $\delta\mathbf{x}$  from its classical site, while:

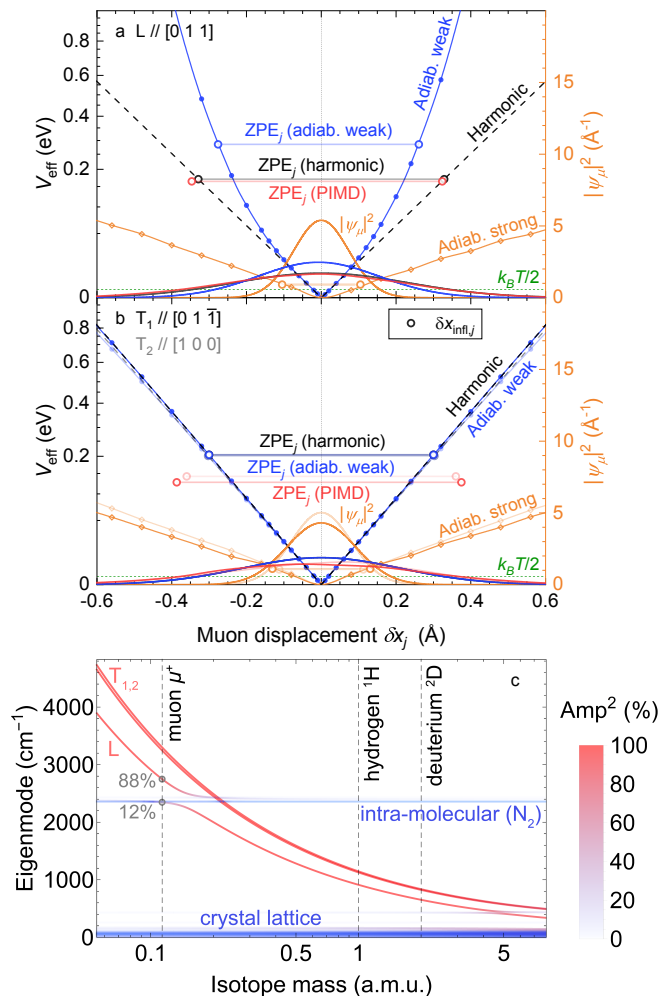


**Fig. 2. Effective muon potential and vibrational spectra.** **a, b** Effective muon potential in a square-root–linear scale (harmonic potentials thus appear as straight lines) along the **a** L and **b** T<sub>1,2</sub> directions for various approximations (left axis) with the corresponding muon probability density function (right axis), directional zero-point energy (ZPE) contributions ZPE<sub>j</sub>, and muon wavefunction inflection points  $\delta x_{\text{infl},j}$ , where  $\partial^2 \psi_\mu / \partial (\delta x_j)^2 = 0$ . Under the harmonic approximation, the muon wavefunction width is  $\Delta x_j = \delta x_{\text{infl},j} / \sqrt{2}$  (see also Table 1). For path-integral molecular dynamics (PIMD) calculations (at  $T = 20$  K), ZPE<sub>j</sub> is estimated as the harmonic ZPE<sub>j</sub> yielding the same  $\Delta x_j$  if  $m_{\text{eff}} = m_\mu$  (Table 1). **c**  $\Gamma$ -point phonon spectra of a supercell of muonated  $\alpha$ -N<sub>2</sub> vs. muon isotope mass  $m_\mu$  [plot generated from a single density functional theory (DFT) calculation; see Methods]. Shading corresponds to the muon amplitude squared in individual normal modes.

(i) keeping the nuclei fixed at the positions corresponding to the unperturbed muon site (weakly-bound case), or (ii) letting them relax by  $\delta \mathbf{r}_N(\delta \mathbf{x})$  to new lowest-energy positions for each  $\delta \mathbf{x}$  (strongly-bound case) while keeping the center of mass fixed. Respectively, this corresponds to: (i) assuming independent muon and nuclear ZPM [i.e., a separable muon–nuclear wavefunc-

tion,  $\psi(\delta\mathbf{x}, \delta\mathbf{r}_N) = \psi_\mu(\delta\mathbf{x})\psi_N(\delta\mathbf{r}_N)$  in the weakly-bound case, or (ii) ZPM where a quantum measurement of the muon displacement  $\delta\mathbf{x}$  would simultaneously also determine all nuclear displacements  $\delta\mathbf{r}_N$  [i.e., a maximally-entangled muon–nuclear wavefunction,  $\psi(\delta\mathbf{x}, \delta\mathbf{r}_N) \propto \psi_\mu(\delta\mathbf{x})\delta(\delta\mathbf{r}_N - \delta\tilde{\mathbf{r}}_N(\delta\mathbf{x}))$ , where  $\delta$  is the Dirac delta function] in the strongly-bound case. Although, by the variational principle, the strongly-bound potential is shallower than the weakly-bound potential (which would tend to increase muon delocalization), the effective mass  $m_{\text{eff}}$  in the strongly-bound case increases above the free-muon mass  $m_\mu$  due to additional movement of nuclei with the muon (which would tend to decrease muon delocalization), meaning that muon ZPM delocalization can either increase or decrease in the strongly-bound case. Explicitly, assuming a linear dependence of the displacement of the  $i$ th nucleus of mass  $m_i$  on the muon displacement, i.e.,  $\delta\tilde{\mathbf{r}}_{N_i}(\delta\mathbf{x}) = A_i\delta\mathbf{x}$  where  $A_i$  is a tensor, the effective mass tensor in the strongly-bound case is given by  $m_{\text{eff}} = m_\mu\text{id} + \sum_i m_i A_i^T A_i$  where  $\text{id}$  is the identity tensor. In the weakly-bound case,  $m_{\text{eff}} = m_\mu$ . Once  $V_{\text{eff}}(\delta\mathbf{x})$  and  $m_{\text{eff}}$  are known, a single-particle Schrödinger equation for the muon wavefunction  $\psi_\mu(\delta\mathbf{x})$ ,  $[-\hbar^2/(2m_{\text{eff}})]\nabla^2\psi_\mu + V_{\text{eff}}\psi_\mu = (\text{ZPE})\psi_\mu$ , can be numerically solved to obtain the muon–nuclear ZPM, encoded in  $\psi_\mu(\delta\mathbf{x})$ , and the corresponding ZPE. This inherently single-particle approximation with 3 degrees of freedom in  $\delta\mathbf{x}$  (due to the assumed zero or maximal muon–nuclear entanglement) cannot describe many-body ZPM involving more than 3 degrees of freedom (i.e., cases with partial muon–nuclear entanglement).

Fig. 2a, b show the calculated weakly- and strongly-bound adiabatic effective potentials. Separable potentials are assumed with one eigenaxis, L  $\parallel [0, 1, 1]$ , along the  $[\text{N}_2-\mu-\text{N}_2]^+$  complex and two,  $\text{T}_1 \parallel [0, 1, \bar{1}]$  and  $\text{T}_2 \parallel [0, 0, 1]$ , transverse to it, coinciding with muon  $\Gamma$ -point normal mode directions from DFT (Fig. 2c). Table 1 lists the total muon ZPE =  $\sum_j \text{ZPE}_j$  with directional contribution  $\text{ZPE}_j$  and muon wavefunction widths  $\Delta x_j = \langle \delta x_j^2 \rangle^{1/2}$  along the  $j = \text{L}, \text{T}_1$ , and  $\text{T}_2$  directions under both approximations. In the weakly-bound case, we find muon ZPM delocalization of 0.16–0.20 Å, which is significant compared to the 1.29(1) Å distance between the classical muon site and the nearest nitrogen. However, in the strongly-bound case we also find large directional effective muon mass renormalization  $m_{\text{eff},j}/m_\mu$  due to strong electrostatic interactions within the  $[\text{N}_2-\mu-\text{N}_2]^+$  complex and with the surrounding polaron, which leads to a large number of nitrogen nuclei following the displaced muon (up to  $494m_\mu$  in the complex and a further  $494m_\mu$  just in first shell of the polaron). This leads to a significantly reduced ZPE and delocalization (Table 1) under the strongly-bound approximation, despite a shallower effective potential (Fig. 2a, b) compared to the weakly-bound case.

## Toy model

Given the discrepancy between the two adiabatic approximations, the question of their applicability arises. In other words, whether muon–nuclear ZPM is minimally (weakly-bound limit), maximally (strongly-bound limit), or partially entangled. We address this using a toy model with the muon bound to  $N = 2$  nearby effective nuclei with force constants  $k_\mu$ , which are further bound to a static lattice with force constants  $k_n$ . If  $k_\mu \ll k_n$  muon displacements barely perturb the nuclei (weakly-bound limit), while if  $k_\mu \gg k_n$  muon displacements strongly displace nearby nuclei (strongly-bound limit). We estimate the ratio  $k_\mu/k_n$  in  $\alpha\text{-N}_2$  from the ratio of adiabatic potentials as  $k_{\mu,j}/k_{n,j} = V_{\text{eff}}^{\text{weak}}/V_{\text{eff}}^{\text{strong}} - 1 \approx 7, 12$ , and  $9$  along the  $j = \text{L}, \text{T}_1$ , and  $\text{T}_2$  directions, respectively (Fig. 2a, b). This excludes the weakly- but not the strongly-bound adiabatic approximation. However, the relatively large ratio  $k_\mu/k_n$  still competes with the tendency of light particles to partially positionally decouple from heavier particles<sup>23</sup>, which could lead to an intermediate, partially-entangled regime where single-particle (adiabatic) approximations fail. This tendency is expected to be further reinforced by the enhanced mass  $m_{n,j}$  of effective nearest nuclei in the toy model needed to obtain the same calculated effective muon mass  $m_{\text{eff},j}$  under the strongly-bound adiabatic approximation both from DFT (Table 1) and from the toy model. Namely, in the toy model we need  $m_{n,j} = (1 + k_{n,j}/k_{\mu,j})^2(m_{\text{eff},j} - m_\mu)/N = 4.2(9)m_N, 1.7(2)m_N$ , and  $2.6(4)m_N$  along the  $j = \text{L}, \text{T}_1$ , and  $\text{T}_2$  directions, respectively, where  $m_N$  is the mass of a nitrogen nucleus.

## Harmonic quantum approximations

An alternative class of approximations are harmonic methods<sup>20,30,31</sup>, which work in the many-body regime of partial entanglement, but are limited to strictly harmonic muon–nuclear interactions. These start with a  $\Gamma$ -point DFT phonon calculation in the classical muon site geometry (a muon is a localized defect and thus has no  $q$ -space dispersion). The usual assumption that, since muons are lighter than nuclei, muon ZPM is fully adiabatically decoupled from the lattice (yielding 3 highest-frequency normal modes  $\omega_j$  describing single-particle muon ZPM; see Fig. 2c), corresponds to the weakly-bound (zero entanglement) adiabatic limit described above, but with the additional constraint of a harmonic adiabatic potential  $V_{\text{eff}}$ . This assumption yields directional ZPE contributions  $\text{ZPE}_j = \hbar\omega_j/2$  and directional ZPM delocalization  $\Delta x_j = \sqrt{\hbar/(2m_\mu\omega_j)}$ . The  $>40\%$  discrepancy between the harmonic and anharmonic weakly-bound adiabatic values of  $\Delta x_L$  thus obtained (Table 1) hints at a breakdown of the harmonic approximation due to strong anharmonicity (Fig. 2a).

Although the weakly-bound adiabatic limit is exact if  $m_\mu \rightarrow 0$ , it cannot reproduce non-zero muon–nuclear entanglement. In fact, in  $\alpha\text{-N}_2$  we see strong hybridization of the L muon normal mode with intra-molecular vibrations of both  $\text{N}_2$  molecules in the  $[\text{N}_2-\mu-\text{N}_2]^+$  com-

**Table 1. Muon zero-point motion parameters in  $\alpha$ -N<sub>2</sub>.** Total muon zero-point energy (ZPE) with directional contributions ZPE<sub>*j*</sub>, muon wavefunction widths  $\Delta x_j$ , and effective muon mass renormalization  $m_{\text{eff},j}/m_\mu$  along the  $j = \text{L}, \text{T}_1$ , and  $\text{T}_2$  directions, in this order, for the approximations described in the text. Path-integral molecular dynamics (PIMD) ZPE<sub>*j*</sub> was estimated as the harmonic ZPE<sub>*j*</sub> yielding the same  $\Delta x_j$  if  $m_{\text{eff}} = m_\mu$  is assumed (marked with \*).

Approximation	ZPE (eV)	ZPE <sub><i>j</i></sub> (eV)	$\Delta x_j$ (Å)	$m_{\text{eff},j}/m_\mu$
Adiabatic (weakly-bound)	0.69	[0.29, 0.20, 0.20]	[0.16, 0.21, 0.21]	1
Adiabatic (strongly-bound)	0.008(4)	[0.0021, 0.0031, 0.0028]	[0.074(4), 0.093(3), 0.079(4)]	[810(160), 350(40), 520(80)]
Harmonic (weakly-bound)	0.58	[0.17, 0.20, 0.20]	[0.23, 0.21, 0.21]	1
PIMD	0.43(11)*	[0.16(11), 0.13(1), 0.14(1)]*	[0.24(8), 0.27(1), 0.25(1)]	1*

plex due to a finite muon mass (Fig. 2c), which implies significant muon–nuclear entanglement<sup>49,50</sup>. This is detected by projecting the top 3 (normalized) phonon normal modes onto pure muon motion, summing the squared norms of the resulting (projected) phonon eigenvectors, and subtracting the value 3, which is expected when muon normal modes do not mix with the lattice modes (i.e., in the weakly-bound limit). This defines an entanglement witness<sup>33–35</sup>  $w_1$  as  $w_1 = 0$  for zero muon–nuclear entanglement (weakly-bound adiabatic limit) and  $w_1 < 0$  in the entangled, many-body case. For muons in  $\alpha$ -N<sub>2</sub> we obtain  $w_1 = -0.14 < 0$ . This again suggests that the weakly- (and possibly also the strongly-) bound adiabatic approximation should fail, as muon–nuclear ZPM is inherently many-body, at least in the harmonic approximation. Were it not for strong anharmonicity, which invalidates the approach, such complex ZPM could still be treated by the full, many-body harmonic method by considering the entire supercell  $\Gamma$ -point phonon spectrum.

### Full quantum muon description

Finally, we turn to numerically-exact PIMD for calculating observables from arbitrary muon–nuclear ZPM<sup>1–3</sup>, based on discretizing imaginary-time,  $T > 0$ , path integrals. Unlike approximate methods, PIMD works even in the anharmonic many-body regime with partial muon–nuclear entanglement<sup>51</sup>. Using PIMD we find that the projected muon probability density is unimodal in  $\alpha$ -N<sub>2</sub> (Fig. 2a, b), confirming that the muon site is unique even for quantum muons<sup>44</sup>, with no signs of quantum tunneling. Thoroughly testing PIMD convergence of observables against simplified toy-model simulations, we confirm that all observables are well converged by  $P = 16$ – $24$  PIMD beads (imaginary-time steps), except for muon ZPM delocalization  $\Delta x_j$ , where we can correct for finite- $P$  effects via a careful  $P \rightarrow \infty$  extrapolation scheme (see Methods and Figs. S3 and S4). We find that muon  $\Delta x_{\text{L}}$  is large enough (Table 1) that anharmonic effects become significant (Fig. 2a) and harmonic approximations fail. Furthermore, all  $\Delta x_j$  are larger than in the weakly- and strongly-bound adiabatic approximations, implying partial muon–nuclear entanglement and many-body ZPM outside of the scope of single-particle approximations, as already anticipated from L normal mode hybridization

**Table 2. Quadrupolar coupling constant of  $\alpha$ -N<sub>2</sub>.** Static nuclear quadrupolar coupling constant (NQCC)  $C_{\text{Q}}^0$  of <sup>14</sup>N in  $\alpha$ -N<sub>2</sub> from uncalibrated density functional theory (DFT) calculations, and calculations calibrated by  $f_{\text{cal}}$  obtained from fits of experimental quadrupolar level-crossing resonance (QLCR) spectra with predictions for a classical (density functional theory, DFT) or a quantum muon (path-integral molecular dynamics, PIMD; see Fig. 3). Discrepancy from the literature value  $-5.39(5)$  MHz<sup>40</sup> is given in standard deviations  $\sigma$ .

Calibration	$T$ (K)	$f_{\text{cal}}$	$C_{\text{Q}}^0$ (MHz)	Discrepancy ( $\sigma$ )
None		1	-5.76	-7.4(2)
Classical $\mu^+$	1.8	1.106(7)	-5.21(3)	3.1(6)
	5	1.103(4)	-5.22(2)	3.2(7)
Quantum $\mu^+$	1.8	1.076(6)	-5.35(3)	0.7(1)
	5	1.073(4)	-5.37(2)	0.4(1)

(Fig. 2c). To quantify the degree of entanglement we calculate a multivariate Pearson correlation coefficient<sup>52</sup>

$$c_i = \frac{\langle \delta \mathbf{x}' \cdot \delta \mathbf{r}'_{\text{Ni}} \rangle}{\sqrt{\langle |\delta \mathbf{x}'|^2 \rangle \langle |\delta \mathbf{r}'_{\text{Ni}}|^2 \rangle}} \in [-1, 1] \quad (1)$$

between the centered muon displacement  $\delta \mathbf{x}' = \delta \mathbf{x} - \langle \delta \mathbf{x} \rangle$  and the centered displacement  $\delta \mathbf{r}'_{\text{Ni}} = \delta \mathbf{r}_{\text{Ni}} - \langle \delta \mathbf{r}_{\text{Ni}} \rangle$  of a nucleus  $i$ , via PIMD. The quantity  $w_{2i} = -|c_i| \in [-1, 0]$  is a witness of muon–nuclear entanglement<sup>33–35</sup>, since  $w_{2i} = 0$  for separable (weakly-bound) states (as then  $\langle \delta \mathbf{x}' \cdot \delta \mathbf{r}'_{\text{Ni}} \rangle = \langle \delta \mathbf{x}' \rangle \cdot \langle \delta \mathbf{r}'_{\text{Ni}} \rangle = 0$ ), which means that  $w_{2i} < 0$  implies entanglement. On the other hand, in the strongly-bound case (maximal entanglement) with  $\delta \tilde{\mathbf{r}}_{\text{Ni}} \propto \delta \mathbf{x}$  we find  $|c_i| = 100\%$ . In  $\alpha$ -N<sub>2</sub> the degree of muon–nuclear entanglement is  $c_i \approx 30(4)\%$  with the two nearest nitrogen nuclei, and decays with distance (Fig. 1c). This confirms that muon–nuclear ZPM in  $\alpha$ -N<sub>2</sub> is partially entangled and thus inherently many-body. We note that a many-body harmonic approximation calculation<sup>29,50</sup> would yield a similar  $c_i$  ( $\approx 26\%$ ) between the muon and the two nearest nitrogen nuclei.

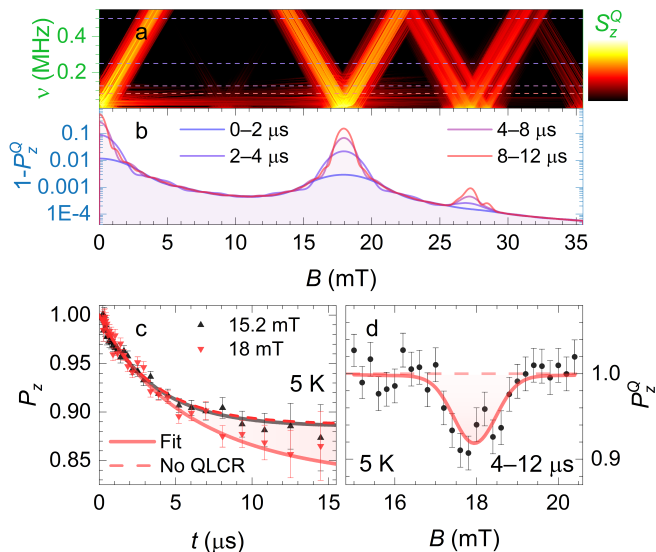


**Fig. 3. Muon quadrupolar level-crossing resonance spectra and fits.** **a** Calibrated Fourier-transformed quadrupolar level-crossing resonance (QLCR) spectra  $S_z^Q(\nu, B)$  vs. frequency  $\nu$  from path-integral molecular dynamics (PIMD) calculations with 24 beads (see Methods) for time-differential QLCR analysis<sup>39</sup>. **b** Muon-lifetime weighed integrals of  $1 - P_z^Q(t, B)$  over different time windows for integral QLCR analysis. **c** Experimental QLCR data at 5 K on (18 mT) and off resonance (15.2 mT) and the global fit with (solid) and without the QLCR term (dashed). **d** Global fit of 5 K QLCR data with PIMD predictions integrated over a 4–12  $\mu\text{s}$  time window vs.  $B$ . Error bars on **c** and **d** represent a statistical uncertainty of one standard deviation.

### QLCR measurements and NQCC of $\alpha\text{-N}_2$

Detailed knowledge of the many-body muon–nuclear ZPM afforded by PIMD allows us to derive an important constant: the static NQCC of  $^{14}\text{N}$  in  $\alpha\text{-N}_2$ , defined as  $C_Q^0 = e_0^2 q_0 Q / h$ , where  $Q = 2.044(3) \text{ fm}^2$  is the quadrupolar moment of  $^{14}\text{N}$ <sup>42,53</sup>, and  $q_0$  is the largest eigenvalue of the electric field gradient (EFG) eigenvalue at the  $^{14}\text{N}$  position, assuming static classical nitrogen nuclei. The experimental NQCC at  $T = 0$ ,  $C_Q = f(0)C_Q^0$ , is reduced from the static  $C_Q^0$  by the solid-nitrogen order parameter  $f(0) = 0.863(8) < 1$  due to the ZPM of nitrogen nuclei<sup>40</sup>. Using DFT we calculate  $C_Q^0$  by assuming classical point-particle nuclei in pristine  $\alpha\text{-N}_2$ , obtaining the *ab initio* value  $C_Q^{0,\text{DFT}} = -5.76 \text{ MHz}$ , which differs from the accepted experimental value  $C_Q^0 = -5.39(5) \text{ MHz}$  by  $\approx 6.9\%$  or  $\approx 7.4$  standard deviations  $\sigma$  (Table 2). The discrepancy arises from systematic errors in DFT calculations of EFGs, which are apparently overestimated by a factor  $f_{\text{cal}} = C_Q^{0,\text{DFT}} / C_Q^0 \approx 1.07(1)$ . To obtain an independent estimate of  $C_Q^0 = f_{\text{cal}}^{-1} C_Q^{0,\text{DFT}}$  we therefore need to determine  $f_{\text{cal}}$ , and calibrate our *ab initio* results against experiment.

To achieve this we performed precision QLCR  $\mu\text{SR}$  measurements on  $\alpha\text{-N}_2$ . In a QLCR experiment muons

stop near  $I \geq 1$  nuclei (here  $^{14}\text{N}$ ), while a longitudinal magnetic field  $B$  is swept in small steps at a given  $T$  and the muon polarization  $P_z(t)$  is measured. For  $B$  where the Zeeman splitting of muon spin energy levels approaches the splitting of nuclear energy levels due to EFGs at nuclear positions, resonant cross-relaxation of muon–nuclear spins occurs, resulting in a sharp dip of the measured late-time  $P_z(t)$ <sup>37–39</sup>. If we also have a good description of muon–nuclear ZPM (e.g., via PIMD), which shifts and reshapes QLCR spectra  $P_z(t, B)$ , we can extract muonated-sample EFGs and compare them to *ab initio* DFT predictions of them to find the sought after DFT calibration factor  $f_{\text{cal}}$ . Since our modeling showed strongly time-window-dependent widths of QLCR spectral peaks in  $\alpha\text{-N}_2$  (Fig. 3b), we went beyond conventional integral or differential QLCR analysis<sup>39</sup>, and performed a simultaneous fit to our data over all measured  $B$  and  $t < 18 \mu\text{s}$  (no binning with a 16 ns time resolution), at each measured  $T$ , using a simple global model

$$P_z(t, B) = A_Q P_z^Q(t, B) + A_{\text{Mu}} e^{-\lambda_{\text{Mu}} t} + A_{\text{bgd}}(B) \quad (2)$$

where  $A_Q$  is the amplitude of QLCR signal,  $P_z^Q$  is the *ab initio* simulated QLCR signal (for either the classical or the quantum case; see Methods) at a given  $f_{\text{cal}}$ , which was a fit parameter (Fig. 3a, b, and Supplementary Fig. 6), while  $A_{\text{Mu}}$  describes the muonium fraction, known to form in  $\alpha\text{-N}_2$ <sup>48</sup> and relaxing with rate  $\lambda_{\text{Mu}}$ . The contribution  $A_{\text{bgd}}(B)$  due to muons stopped outside the sample was modeled as a constant plus a weak Lorentzian of  $B$ , with fits yielding a field variation of  $< 10\%$  of the QLCR signal (Fig. 3c), which does not affect our conclusions. These fits described  $> 28,000$  experimental data points at each  $T$  using only 8 global fit parameters (Fig. 3c, d), with good fit quality (see Methods) and without systematic deviations at any  $t$  or  $B$  (Supplementary Fig. 5). This held true for both classical and quantum cases, as the main effect of muon–nuclear ZPM was a simple shift of the main QLCR peak, which was absorbed into the fitted value of  $f_{\text{cal}}$ . Extracting  $f_{\text{cal}}$  from fits of QLCR spectra under the classical muon ansatz we thus obtain  $C_Q^0 = f_{\text{cal}}^{-1} C_Q^{0,\text{DFT}} = -5.22(2) \text{ MHz}$ , which still differs from the accepted experimental value by  $\approx 3.2\sigma$  (Table 2). However, extracting  $f_{\text{cal}}$  from fits of QLCR spectra using a PIMD description of muon–nuclear ZPM, which is well-converged without the need for finite- $P$  extrapolation (see Methods and Supplementary Fig. 3), we obtain excellent agreement with previous experiments, with the final value  $C_Q^0 = -5.36(2) \text{ MHz}$  (Table 2) statistically even more accurate than the previous best estimate of  $-5.39(5) \text{ MHz}$ <sup>40</sup>.

### DISCUSSION

Based on the above analysis we are able to propose several rules of thumb for when to expect quantum muon effects, which have the potential to significantly impact the interpretation of  $\mu\text{SR}$  experiments. Many-body quantum muon effects are expected to be large whenever: (i) the muon is strongly (chemically) bound to the crystal lattice

(see Toy model), e.g., when the material is ionic or contains very electronegative atoms, like  $F^-$ ,  $Cl^-$ ,  $Br^-$ ,  $O^{2-}$ , or  $N^{3-}$ , or functional groups, like  $OH^-$ , that strongly attract the muon, or (ii) when the phonon normal modes of the pristine material are high-frequency, allowing them to hybridize with muon normal modes (Fig. 2c). For example, the latter scenario is expected when the local chemical bonds in the material around the muon site are strong, e.g., ionic or strong covalent (e.g., double or triple) bonds, or when the material contains light atoms; especially if the bonds are weaker further away from the muon site, like in molecular crystals, as discussed in the Toy model section. Under the same conditions, muon ZPE is expected to be high, which could affect the energy ordering, and thus the expected occupancy, of candidate muon sites. These same conditions are also expected to lead to strong deformations of the crystal structure around the muon sites, which suggests a simple rule: if the muon strongly perturbs the crystal structure classically, it likely also becomes quantum entangled with it with a high ZPE. On the other hand, anharmonic quantum muon effects are expected to be important when: (i) the muon is highly delocalized, which occurs when it is weakly bound to neighboring atoms, e.g., at interstitial sites, or, alternatively, (ii) if the effective muon potential is inherently highly anharmonic (Fig. 2a). Muon delocalization and anharmonicity can strongly affect the interpretation of  $\mu$ SR results, since they directly affect the nature and strength of the coupling of the muon to the local magnetic fields. When either just many-body or anharmonic effects are present, they can be treated using appropriate harmonic or adiabatic approximations, respectively. However, as seen in the case of muons in  $\alpha$ -N<sub>2</sub>, many-body and anharmonic effects can also be present at the same time requiring their careful examination using more general quantum methods. Examples of these include numerically-exact methods like PIMD or the recently-proposed many-interacting-worlds approach<sup>54,55</sup>. We note that the discussion above is independent of the local symmetry, or any lack thereof, at the muon site.

Beyond muons, our unified description of light-particle ZPM, where quantum regimes with well-defined approximations arise in certain limits of particle-lattice entanglement and anharmonicity, directly applies also to other light particles and light-atom nuclei, e.g., hydrogen and lithium, in solids. Such an extension is of immense interest, as nuclear quantum effects were shown to play a crucial role, for example, in stabilizing recent record high- $T_c$  hydride superconductors H<sub>3</sub>S<sup>4,56,57</sup> and LaH<sub>10</sub><sup>5,58,59</sup>, as well as the contentious supposed room-temperature superconductors LuH<sub>3- $\delta$</sub> N <sub>$\epsilon$</sub> <sup>6,7</sup> and CSH<sub>8</sub><sup>8-10,60</sup>, and in explaining their huge isotope effects, as calculated via the self-consistent harmonic approximation<sup>56,57,59</sup>. A similar situation arises in the recent record-density hydrogen storage material (CH<sub>4</sub>)<sub>3</sub>(H<sub>2</sub>)<sub>25</sub><sup>11</sup>, which was found to be stabilized by nuclear quantum effects via the harmonic approximation, and in calculating solvation free energies

of Li and F<sup>12</sup> via the quasi-harmonic approximation. In all of these materials, a careful examination of the underlying entanglement and anharmonicity regimes of nuclear ZPM using the approaches described in this paper could reveal any possible limitations on the validity of the approximations used and provide a systematic way of finding even more accurate nuclear ZPM descriptions. In this way, our understanding of these highly intriguing quantum materials could be substantially improved.

In conclusion, we have performed an analysis of muon-nuclear ZPM in  $\alpha$ -N<sub>2</sub>, culminating in a precision determination of the static NQCC of <sup>14</sup>N in pristine  $\alpha$ -N<sub>2</sub> using complementary QLCR experiments and state-of-the-art *ab initio* DFT+PIMD calculations, significantly improving the accuracy of this constant over the previously known value. We also discovered an electric-dipole polaron with strong effective mass renormalization around muons in  $\alpha$ -N<sub>2</sub>, which might affect the interpretation of experiments purportedly showing quantum tunneling of muonium in this material<sup>23</sup>. In fact, a similar polaron might generically be expected in molecular crystals with charged impurities. More broadly, our work demonstrates the need to consider quantum effects when interpreting  $\mu$ SR data, paying attention to the presence of muon-nuclear entanglement and anharmonicity, to guide the choice of the applicable ZPM approximation. This unified perspective on light-particle ZPM is generally applicable and should be explored further also in the context of material science and quantum chemistry, where it promises to offer a way of finding accurate and computationally-efficient descriptions of nuclear quantum effects of light atoms across a wide range of quantum materials.

## METHODS

### DFT calculations

Both the pristine and muonated low- $T$  low-pressure  $\alpha$  phase of solid nitrogen,  $\alpha$ -N<sub>2</sub>, was studied using the CASTEP plane-wave *ab initio* density functional theory (DFT) code<sup>61</sup> using the PBE exchange-correlation functional<sup>62</sup> and ultrasoft pseudopotentials. Calculations were carried out on a  $2 \times 2 \times 2$  supercell to avoid finite-size effects around the implanted muon, while a 1200 eV plane-wave energy cutoff and  $2 \times 2 \times 2$  Monkhorst-Pack grid<sup>63</sup> reciprocal-space sampling was chosen to achieve numerical convergence. A neutral cell was used for pristine structure calculations, while a positive elementary charge per supercell was applied in calculations of muonated structures, to account for the positive charge of the muon. All calculations were converged to within a total energy tolerance of 0.1 meV/atom in the self-consistent field (SCF) DFT loop, while geometry relaxation tasks were converged to within a tight 5 meV  $\text{\AA}^{-1}$  force tolerance on the muon and nuclei. Furthermore, to properly account for weak cohesive van der Waals (VdW) dispersion forces between N<sub>2</sub> molecules, which are usually underestimated in pure DFT, a Tkatchenko-Scheffler (TS) semi-empirical dispersion correction scheme was applied in a DFT-D approach<sup>64</sup>. We note, though, that the results of ordinary DFT with an *ad hoc* isotropic external hydrostatic pressure of 0.5 GPa (chosen to reproduce the experimental zero-pressure unit cell volume of pristine  $\alpha$ -N<sub>2</sub>) were practically indistinguishable from the results of full DFT-D calculations, even in the presence of an implanted muon. This indicates

that in  $\alpha$ -N<sub>2</sub> the dominant VdW dispersion force contribution is a simple isotropic attraction among all nuclei and the muon.

Despite competing suggestions of a  $Pa\bar{3}$  (No. 205) or a  $P2_13$  (No. 198) cubic crystallographic structure of pristine  $\alpha$ -N<sub>2</sub> in the literature<sup>40</sup>, we find that the higher-symmetry  $Pa\bar{3}$  structure is moderately preferred in our DFT calculations (by  $\sim 0.05$  eV per unit cell), in line with recent consensus<sup>41,42,65</sup>. In this structure the centers of N<sub>2</sub> molecules form a face-centered cubic lattice (Supplementary Fig. 1a).

### Classical muon stopping site

To find candidate muon stopping sites in  $\alpha$ -N<sub>2</sub> a muon's initial position was randomly seeded in the unit cell and the full crystal geometry (including the muon position) relaxed at a fixed, experimental cell volume until convergence. This process was repeated  $>20$  times to generate a list of candidate muon stopping sites, which were then grouped into clusters by identifying those candidate muon sites within  $<0.7$  Å of each other (or of any in-between sites) as belonging to the same cluster. Here the distance between two arbitrary candidate muon sites  $\mathbf{r}_{\mu 1}$  and  $\mathbf{r}_{\mu 2}$  was taken as the minimal possible real-space distance  $|\mathbf{r}_{\mu 1} - T\mathbf{r}_{\mu 2}|$  under any symmetry operation  $T$  in the pristine  $\alpha$ -N<sub>2</sub> crystallographic space group  $Pa\bar{3}$  (including discrete translational, rotational and reflection symmetries). This is because the implanted muon is the sole source of local symmetry breaking in the crystal and thus muon sites related by pristine space-group symmetry operations should be regarded as identical. A muon site cluster can thus be thought of as a connected component in a graph whose vertices are the calculated muon sites that are considered adjacent if their minimal, symmetry-reduced distance is below a chosen threshold (0.7 Å in our case). We note that this symmetry-aware clustering algorithm based on graph theory is also implemented in the user-friendly MuFinder program for determining and analysing muon stopping sites<sup>19,25</sup>. In the end, we find a single muon site cluster in  $\alpha$ -N<sub>2</sub>, which lies at the point midway between the centers of the two neighboring N<sub>2</sub> molecules of the pristine  $\alpha$ -N<sub>2</sub> structure (Supplementary Fig. 1b).

$\Gamma$ -point phonon spectra were calculated on a  $2 \times 2 \times 2$  supercell of  $\alpha$ -N<sub>2</sub>, with the whole isotope effect plot (Fig. 2c) generated from a single DFT calculation of phonon normal modes and frequencies. This was achieved by first reconstructing the dynamical matrix (DM)<sup>49,50</sup> of the muonated crystal, reweighting it by the desired muon isotope mass  $m_\mu$ , and then re-diagonalizing it to obtain the new phonon normal modes and frequencies.

### Choice of the exchange–correlation functional

We note that switching to an *a priori* less accurate local density approximation (LDA) DFT exchange–correlation functional<sup>61</sup> does not significantly alter our results. Namely, the classical muon–nuclear distance in the  $[\text{N}_2 - \mu - \text{N}_2]^+$  complex changes by just  $-0.01$  Å, the total harmonic ZPE of the 3 highest-frequency (muon) normal modes changes by  $+4.1\%$  compared to the PBE functional, and the harmonic (under)estimate of the entanglement coefficient  $c_i$  of the muon with the two nearest nitrogen nuclei changes from  $\approx 26\%$  to  $\approx 24\%$ . The anharmonicity measure  $V_{\text{eff}}^{\text{weak}}(2\delta\mathbf{x}) / (4V_{\text{eff}}^{\text{weak}}(\delta\mathbf{x}))$ , which would equal 1 for a purely harmonic potential, at a typical displacement  $2\delta x = +0.24$  Å along the most anharmonic direction L (Fig. 2a) changes slightly, from 1.8 to 1.6, when switching from PBE to LDA. Many-body and anharmonic ZPM effects of muons in  $\alpha$ -N<sub>2</sub> are thus rather robust against the choice of the exchange–correlation functional. Nevertheless, we used PBE for all the results reported in the manuscript, as described above, since it is in general expected to be much more accurate than LDA for describing electronic systems, such as  $\alpha$ -N<sub>2</sub>, where electrons are not highly correlated.

### Classical MD and quantum PIMD calculations

For PIMD calculations an NVT statistical ensemble of up to  $P = 32$  beads was simulated for up to  $S = 8,600$  steps of 0.5 fs with a  $T = 20$  K stochastic Langevin thermostat. Satisfactory convergence in bead number was achieved already for  $P = 16$ –24 beads for all QLCR resonance parameters (Supplementary Fig. 3) and positional observables (Supplementary Fig. 4) except for the muon wavefunction widths (Supplementary Fig. 4a), which had to be extrapolated to the  $P \rightarrow \infty$  limit (see heading Extrapolation of PIMD muon widths). Classical MD simulations (which can be interpreted as  $P = 1$  PIMD simulations) used the same statistical ensemble, time step, temperature, and thermostat and were run for up to  $S = 12,000$  steps. Care was taken to ensure proper thermalization of the ensembles before observables were extracted from them.

Both PIMD and MD simulations produce a list of  $SP$  muon–nuclear configurations  $\{\mathbf{r}_i^{(s,p)}\}_{i=1}^K$ , where  $s = 1, \dots, S$  is the time step,  $p = 1, \dots, P$  is the bead index, and  $\mathbf{r}_i$  is the position of one muon or nucleus  $i$  out of  $K$  muons and nuclei present in the system. These muon–nuclear configurations follow the corresponding Boltzmann statistical probability distribution for finding muons and nuclei at these positions. In the case of MD this is the  $T > 0$  classical thermal probability distribution  $\rho_c(\mathbf{r}_1, \dots, \mathbf{r}_K)$ , while in PIMD this is the quantum thermal probability distribution  $\rho_q(\mathbf{r}_1, \dots, \mathbf{r}_K)$ , which at  $T = 0$  would coincide with the ground-state wavefunction's  $|\psi\rangle$  probability distribution  $\rho_q(\mathbf{r}_1, \dots, \mathbf{r}_K) = |\psi(\mathbf{r}_1, \dots, \mathbf{r}_K)|^2$ . The thermal expectation value  $\langle O \rangle$  of any observable  $O$  that depends only on muon–nuclear positions can thus be approximated from numerical PIMD or MD samples by calculating the average

$$\langle O \rangle \approx \frac{1}{SP} \sum_{s=1}^S \sum_{p=1}^P O(\mathbf{r}_1^{(s,p)}, \dots, \mathbf{r}_K^{(s,p)}) \quad (3)$$

For observables that were expensive to calculate [e.g., the electric field gradients (EFG), which require a full DFT calculation for each muon–nuclear configuration in the above average] a further Monte Carlo approximation to the average was employed by randomly sampling only a small number of  $s$  and  $p$  ( $\approx 120$  in the case of EFGs) in Eq. (3). For certain numerically-noisy observables, like the directional wavefunction widths in Table 1, multiple runs at a given  $P$  were merged together to improve statistics and provide a more reliable numerical estimate.

### ZPM and quantum entanglement from PIMD

A numerical estimate of the average position  $\langle \mathbf{r}_i \rangle$  of a given muon or nucleus  $i$  can be calculated in this way by choosing  $O(\mathbf{r}_1, \dots, \mathbf{r}_K) = \mathbf{r}_i$  in Eq. (3). From this we can estimate the squared gyration radius  $\Delta r_i^2 = \langle |\delta \mathbf{r}_i|^2 \rangle = \langle |\mathbf{r}_i - \langle \mathbf{r}_i \rangle|^2 \rangle$ , which corresponds to choosing  $O = |\mathbf{r}_i - \langle \mathbf{r}_i \rangle|^2$ , and the covariance  $\langle \delta \mathbf{r}_i \cdot \delta \mathbf{r}_{i'} \rangle$  by choosing  $O = (\mathbf{r}_i - \langle \mathbf{r}_i \rangle) \cdot (\mathbf{r}_{i'} - \langle \mathbf{r}_{i'} \rangle)$ . Using these we can then extract a numerical estimate of the multivariate Pearson correlation coefficient  $c_{ii'} = \langle \delta \mathbf{r}_i \cdot \delta \mathbf{r}_{i'} \rangle / (\Delta r_i \Delta r_{i'}) \in [-1, 1]$ <sup>52</sup>. If this is non-zero as  $T \rightarrow 0$  it implies ground-state positional entanglement of muons or nuclei  $i$  and  $i'$  (see Results). We can also calculate the squared ZPM delocalization of a muon  $\Delta x_j^2$  along a given direction  $j = L, T_1, T_2$ , by choosing  $O = |(\Delta \mathbf{x} - \langle \Delta \mathbf{x} \rangle) \cdot \hat{\mathbf{v}}_j|^2$  for the corresponding unit vector  $\hat{\mathbf{v}}_j$  along this direction.

### Extrapolation of PIMD muon widths

While the covariance of muon–nuclear positions (Supplementary Fig. 4b), the wavefunction widths of the nitrogen nuclei (Supplementary Fig. 4c), and QLCR resonance parameters (Supplementary Fig. 3) all fully converge for  $P = 16$ –24 beads, the muon wavefunction widths  $\Delta x_j$  do not (Supplementary Fig. 4a).

However, numerical estimates of expected PIMD convergence under the harmonic toy model described in the main text indicate that the muon wavefunction width is expected to be underestimated by the same factor of  $g \approx 0.55(2)$  at  $P = 24$  compared to the  $P \rightarrow \infty$  limit in all three directions  $j$  (Supplementary Fig. 4a). This allows us to estimate the true values of  $\Delta x_j$  in the  $P \rightarrow \infty$  limit (Table 1) by dividing the raw PIMD values  $\Delta x_j = 0.13, 0.15,$  and  $0.14 \text{ \AA}$  along the L, T<sub>1</sub>, and T<sub>2</sub> directions, respectively, by this factor  $g$ . Moreover, as these widths feature in the multivariate Pearson correlation coefficient  $c_i$  in Eq. (1), we estimate the true values of this entanglement proxy  $c_i$  in the  $P \rightarrow \infty$  limit (Fig. 1c) by multiplying raw PIMD values by the same factor  $g$ .

As this procedure mostly neglects anharmonic effects, which are relevant along the  $j = \text{L}$  direction, we estimate the additional relative systematic uncertainty due to this omission along the direction  $j = \text{L}$  from the relative difference of  $\Delta x_j$  values in the anharmonic weakly-bound adiabatic approximation and the harmonic approximation (Table 1), as a proxy for the influence of anharmonic effects. This yields an additional relative systematic uncertainty of at most  $\approx 30\%$  in the muon wavefunction width along the  $j = \text{L}$  direction, and  $\approx 10\%$  in the entanglement witness  $c_i$ .

Finally, we note the robustness of this extrapolation scheme, as even the harmonic weakly-bound adiabatic approximation (corresponding to  $N = 0$  dynamical nuclei around the muon in the toy model), which is expected to be much less accurate than the  $N = 2$  toy model for estimating PIMD convergence, yields a similar estimate of  $g \approx 0.47(2)$  at  $P = 24$ .

### Thermal effects and classical MD

Since PIMD calculations require a finite temperature for numerical convergence ( $T = 20 \text{ K}$  in our calculations) we also checked that the observed quantum effects were not masked by thermal excitations by comparing quantum PIMD calculations against complementary classical MD simulations at the same  $T$ . We find that the classical thermal spread of muon–nuclear positions is indeed predicted to be much smaller than the quantum wavefunction widths (Table 1), giving just  $\Delta x_j = 0.08$  and  $0.07 \text{ \AA}$  along  $j = \text{L}$  and T<sub>1,2</sub>, respectively, as can be expected from the steepness of the calculated adiabatic and harmonic effective potentials (Fig. 2a, b) in relation to the thermal equipartition energy  $k_B T/2 = 1.7 \text{ meV}$  at this  $T$ , where  $k_B$  is the Boltzmann constant.

Furthermore, quantum-mechanically a transition from  $T$ -independent ground-state ZPM to thermally-excited,  $T$ -dependent quantum behavior along a given direction  $j$  upon increasing  $T$  is only expected when  $k_B T$  becomes comparable to the splitting  $\Delta E_j$  between the ground-state and the first excited ZPM state. Namely, when  $k_B T \ll \Delta E_j$  the system is effectively frozen in its quantum ground state, in contrast to the classical point-particle prediction of a  $T$ -dependent spread of muon–nuclear positions down to the lowest  $T$ . Under the harmonic approximation this splitting can be obtained as  $\Delta E_j = 2ZPE_j$ , while  $\Delta E_j > 2ZPE_j$  when anharmonicity that increases the effective potential at larger displacements is present, as, e.g., in the case of muons in  $\alpha\text{-N}_2$  along the  $j = \text{L}$  direction (Fig. 2a). From Table 1 we can see that all considered approximations point to muons in  $\alpha\text{-N}_2$  being in the low- $T$ ,  $k_B T \ll \Delta E_j$  regime along all directions  $j$  at the considered temperatures. We thus conclude that thermal effects are irrelevant for muon ZPM in  $\alpha\text{-N}_2$  at these low  $T$ , and that the muon–nuclear system is, in fact, in its  $T$ -independent quantum ground state, at least locally around the muon.

### QLCR spectra calculations

If we were to assume fixed classical muon–nuclear positions  $\{\mathbf{r}_i\}_{i=1}^K$  and the corresponding EFG tensors  $\{V_i\}_{i=1}^K$  at those positions (these can be calculated from the muon–nuclear positions using DFT), the muon and nuclear spins would interact via a Hamiltonian  $H$  composed of a Zeeman contribution  $H_Z$ , a local quadrupolar contribution  $H_Q$ , and a dipole coupling contribution  $H_D$ <sup>37,38,66,67</sup>

$$\begin{aligned} H &= H_Z + H_Q + H_D \\ H_Z &= - \sum_i \gamma_i \hbar \mathbf{S}_i \cdot \mathbf{B} \\ H_Q &= \sum_i \frac{e_0 Q_i}{2S_i(2S_i - 1)} \mathbf{S}_i \cdot V_i \mathbf{S}_i \\ H_D &= \sum_{\langle ii' \rangle} \frac{\mu_0 \gamma_i \gamma_{i'} \hbar^2}{4\pi |\mathbf{r}_{ii'}|^3} [\mathbf{S}_i \cdot \mathbf{S}_{i'} - 3(\mathbf{S}_i \cdot \hat{\mathbf{r}}_{ii'}) (\hat{\mathbf{r}}_{ii'} \cdot \mathbf{S}_{i'})] \end{aligned} \quad (4)$$

where  $\gamma_i$  is the gyromagnetic ratio of muon or nucleus  $i$  with spin vector  $\mathbf{S}_i$ , spin size  $S_i$ , and nuclear quadrupole moment  $Q_i$ ,  $\mathbf{B}$  is the applied magnetic field,  $e_0$  is the elementary charge,  $\mu_0$  is vacuum permeability, the sum in  $H_D$  is over unique pairs of muon or nuclei  $\langle ii' \rangle$ ,  $\mathbf{r}_{ii'} = \mathbf{r}_i - \mathbf{r}_{i'}$  is a vector from a muon or nucleus  $i'$  to  $i$ , and  $\hat{\mathbf{r}}_{ii'} = \mathbf{r}_{ii'}/|\mathbf{r}_{ii'}|$  is a unit vector in the same direction. However, due to both quantum ZPM and thermal movement the muons and nuclei described by this Hamiltonian do not have fixed classical (point-particle) positions, nor are the EFGs independent of those positions.

To reduce the complexity of solving the full, coupled spin–positional Hamiltonian of Eq. (4), we assume that there is no significant entanglement between the spin and spatial degrees of freedom in the  $T \approx 0$  ground-state wavefunction of the system, i.e., that  $|\psi\rangle = |\psi\rangle_{\text{spin}} \otimes |\psi\rangle_{\text{position}}$ , due to a separation of timescales for positional and spin dynamics. In this way we can construct an effective spin-only Hamiltonian operator by averaging out the positional degrees of freedom with a partial trace

$$H_{\text{eff,spin}} = \text{tr}_{\text{position}} \{ \rho H \} \quad (5)$$

where  $\rho$  is the total density matrix, which at  $T = 0$  equals simply  $\rho = |\psi\rangle \langle \psi|$ ; i.e., at  $T = 0$  we have  $H_{\text{eff,spin}} = \text{position} \langle \psi | H | \psi \rangle_{\text{position}}$ . In PIMD and MD simulations this can be done numerically by calculating an average over positional degrees of freedom via Eq. (3) where the observable  $O$  is taken to be the full Hamiltonian  $H$  from Eq. (4), and at each muon–nuclear configuration sample  $\{\mathbf{r}_i^{(s,p)}\}_{i=1}^K$  we recalculate the corresponding EFG tensors  $V_i$  via DFT. As mentioned previously, due to the time complexity of calculating the EFG tensors, the full average in Eq. (3) is approximated via Monte Carlo sampling of  $\approx 120$  random  $s$  and  $p$  indices from the PIMD or MD muon–nuclear configurations  $\{\mathbf{r}_i^{(s,p)}\}_{i=1}^K$ .

The numerical calculation of a single Hamiltonian sample [Eq. (4)] from the muon–nuclear configuration and the corresponding EFG tensors was performed using the CalcALC program<sup>68,69</sup> by considering only the four  $^{14}\text{N}$  nuclei in the  $[\text{N}_2 - \mu - \text{N}_2]^+$  complex, i.e., the four nitrogen nuclei closest to the muon, since further-away nitrogen nuclei are only very weakly dipolarly coupled to the muon and thus do not affect its relaxation much. A  $^{14}\text{N}$  nuclear quadrupole moment of  $Q = 2.044(3) \text{ fm}^2$  was used<sup>42,53</sup>. Once the effective spin-only Hamiltonian [Eq. (5)] was thus calculated via Eq. (3), a CalcALC-inspired Python program was used to calculate the time-dependent muon relaxation signal  $P_z^Q(t)$  due to QLCR via exact diagonalization as in Ref.<sup>70</sup> for a range of applied magnetic fields  $B$ . At this stage, the quadrupolar contribution  $H_Q$  was multiplied by an EFG calibration factor  $f_{\text{cal}}^{-1} \approx 1$ , removing most of the otherwise unavoidable

systematic errors of DFT (see the Results section). In global fits of experimental QLCR spectra  $f_{\text{cal}}$  was adjusted in a loop until convergence to a minimal  $\chi^2$  was achieved. We note that in these fits no systematic deviations at any  $t$  or  $B$  were observed (Supplementary Fig. 5). The total global fit quality was  $\chi^2/\text{DOF} = 1.06$  and 1.08 at  $T = 1.8$  and 5 K, respectively.

The final, calibrated QLCR spectra  $1 - P_z^{\text{Q}}(t, B)$  exhibit a non-trivial dependence on time  $t$  and applied field  $B$  and are shown in Supplementary Fig. 6. Fig. 3a shows their Fourier transforms

$$S_z^{\text{Q}}(\nu, B) = \frac{1}{2\pi} \int_{-\infty}^{\infty} [1 - P_z^{\text{Q}}(t, B)] e^{-2\pi i \nu t} dt \quad (6)$$

under the convention  $P_z^{\text{Q}}(-t, B) = P_z^{\text{Q}}(t, B)$  and where  $\nu$  is the frequency, while Fig. 3b shows their weighted time integrals

$$\bar{P}_z^{\text{Q}}(B) = \frac{\int_{t_1}^{t_2} P_z^{\text{Q}}(t, B) e^{-t/\tau_\mu} dt}{\int_{t_1}^{t_2} e^{-t/\tau_\mu} dt} \quad (7)$$

over select time windows  $t \in [t_1, t_2]$ , weighed by the mean muon lifetime  $\tau_\mu = 2.197 \mu\text{s}$ <sup>71</sup> to account for the exponential decay of muons and their subsequent Poissonian counting statistics in  $\mu\text{SR}$  measurements<sup>15</sup>.

### QLCR measurements

QLCR  $\mu\text{SR}$  measurements on  $\alpha\text{-N}_2$  were performed on the EMU beamline<sup>72</sup> (ISIS pulsed muon source), using a custom-built TiZr gas condensation cell. A 100  $\mu\text{m}$  thick Ti window allowed surface muons to enter the sample volume, while a separate experiment confirmed negligible muon depolarisation in TiZr over the studied  $T$ . A  $^4\text{He}$  exchange gas cryostat around the cell provided control over sample  $T$  down to  $\sim 1.5$  K, while a  $1/8$ " capillary connecting the cell to an external gas supply was heated along its length to avoid blockages. The sample was condensed from high purity (Grade 6.0)  $\text{N}_2$  gas, with  $\approx 1.8$  bar  $\text{L}^{-1}$  of gas being condensed at  $\approx 65$  K to ensure the  $\approx 1.6$   $\text{cm}^3$  sample volume was full. Gas pressure was maintained well above the  $\text{N}_2$  triple point ( $\approx 0.125$  bar) throughout sample condensation to avoid deposition of the gas directly into the solid phase. Once condensation was complete, the sample was cooled through the freezing point at  $\approx 0.6$  K/min, with the form of  $\mu\text{SR}$  spectra recorded at 58 K ( $\beta\text{-N}_2$  phase) compared to earlier data on this system<sup>48</sup>, as well as our higher- $T$  data, to confirm the sample was frozen.

### DATA AVAILABILITY

The data presented in this paper<sup>73</sup> are available at <https://dx.doi.org/10.6084/m9.figshare.23203037>. All other data are available from the corresponding author on reasonable request.

Supplementary Movies 1 and 2 present animated versions of Fig. 1a and Fig. 1b, respectively.

### CODE AVAILABILITY

The computer code used to generate and/or analyse the data in this paper<sup>73</sup> is available at <https://dx.doi.org/10.6084/m9.figshare.23203037>.

### REFERENCES

- C. P. Herrero and R. Ramirez, Path-integral simulation of solids, *J. Phys. Condens. Matter.* **26**, 233201 (2014).
- M. Ceriotti, W. Fang, P. G. Kusalik, R. H. McKenzie, A. Michaelides, M. A. Morales, and T. E. Markland, Nuclear quantum effects in water and aqueous systems: Experiment, theory, and current challenges, *Chem. Rev.* **116**, 7529 (2016).
- T. E. Markland and M. Ceriotti, Nuclear quantum effects enter the mainstream, *Nat. Rev. Chem.* **2**, 1 (2018).
- A. Drozdov, M. Erements, I. Troyan, V. Ksenofontov, and S. I. Shylin, Conventional superconductivity at 203 kelvin at high pressures in the sulfur hydride system, *Nature* **525**, 73 (2015).
- A. Drozdov, P. Kong, V. Minkov, S. Besedin, M. Kuzovnikov, S. Mozaffari, L. Balicas, F. Balakirev, D. Graf, V. Prakapenka, *et al.*, Superconductivity at 250 K in lanthanum hydride under high pressures, *Nature* **569**, 528 (2019).
- N. Dasenbrock-Gammon, E. Snider, R. McBride, H. Pasan, D. Durkee, N. Khalvashi-Sutter, S. Munasinghe, S. E. Dissanayake, K. V. Lawler, A. Salamat, *et al.*, Evidence of near-ambient superconductivity in a N-doped lutetium hydride, *Nature* **615**, 244 (2023).
- X. Ming, Y.-J. Zhang, X. Zhu, Q. Li, C. He, Y. Liu, T. Huang, G. Liu, B. Zheng, H. Yang, *et al.*, Absence of near-ambient superconductivity in  $\text{LuH}_{2\pm x}\text{N}_y$ , *Nature* [10.1038/s41586-023-06162-w](https://doi.org/10.1038/s41586-023-06162-w) (2023).
- E. Snider, N. Dasenbrock-Gammon, R. McBride, M. Debessai, H. Vindana, K. Venkatasamy, K. V. Lawler, A. Salamat, and R. P. Dias, Room-temperature superconductivity in a carbonaceous sulfur hydride, *Nature* **586**, 373 (2020).
- E. Snider, N. Dasenbrock-Gammon, R. McBride, M. Debessai, H. Vindana, K. Venkatasamy, K. V. Lawler, A. Salamat, and R. P. Dias, Retraction note: Room-temperature superconductivity in a carbonaceous sulfur hydride, *Nature* **610**, 804 (2022).
- M. Erements, V. Minkov, A. Drozdov, P. Kong, V. Ksenofontov, S. Shylin, S. Bud'ko, R. Prozorov, F. Balakirev, D. Sun, *et al.*, High-temperature superconductivity in hydrides: experimental evidence and details, *J. Supercond. Nov. Magn.* **35**, 965 (2022).
- U. Ranieri, L. J. Conway, M.-E. Donnelly, H. Hu, M. Wang, P. Dalladay-Simpson, M. Peña Alvarez, E. Gregoryanz, A. Hermann, and R. T. Howie, Formation and stability of dense methane-hydrogen compounds, *Phys. Rev. Lett.* **128**, 215702 (2022).
- T. T. Duignan, M. D. Baer, G. K. Schenter, and C. J. Mundy, Real single ion solvation free energies with quantum mechanical simulation, *Chem. Sci.* **8**, 6131 (2017).
- G. J. Ackland, M. Dunuwille, M. Martinez-Canales, I. Loa, R. Zhang, S. Sinogeikin, W. Cai, and S. Deemyad, Quantum and isotope effects in lithium metal, *Science* **356**, 1254 (2017).
- S. J. Blundell, Spin-polarized muons in condensed matter physics, *Contemp. Phys.* **40**, 175 (1999).
- S. J. Blundell, R. De Renzi, T. Lancaster, and F. L. Pratt, *Muon Spectroscopy: An Introduction* (Oxford University Press, Oxford, 2021).
- A. Yaouanc and P. D. De Réotier, *Muon spin rotation, relaxation, and resonance: applications to condensed matter* (Oxford University Press, Oxford, 2011).
- J. S. Möller, P. Bonfà, D. Ceresoli, F. Bernardini, S. J. Blundell, T. Lancaster, R. D. Renzi, N. Marzari, I. Watanabe, S. Sulaiman, and M. I. Mohamed-Ibrahim, Playing quantum hide-and-seek with the muon: localizing muon stopping sites, *Phys. Scr.* **88**, 068510 (2013).
- P. Bonfà and R. De Renzi, Toward the computational prediction of muon sites and interaction parameters, *J. Phys. Soc. Jpn.* **85**, 091014 (2016).
- B. M. Huddart, *Muon stopping sites in magnetic systems*

- from density functional theory, [Ph.D. thesis](#), Durham University, Durham, UK (2020).
20. S. Mañas-Valero, B. M. Huddart, T. Lancaster, E. Coronado, and F. L. Pratt, Quantum phases and spin liquid properties of 1T-TaS<sub>2</sub>, [npj Quantum Mater.](#) **6**, 1 (2021).
  21. G. Prando, P. Bonfà, G. Profeta, R. Khasanov, F. Bernardini, M. Mazzani, E. M. Brünig, A. Pal, V. P. S. Awana, H.-J. Grafe, B. Büchner, R. De Renzi, P. Carretta, and S. Sanna, Common effect of chemical and external pressures on the magnetic properties of RCoPO ( $R = \text{La, Pr}$ ), [Phys. Rev. B](#) **87**, 064401 (2013).
  22. I. J. Onuorah, P. Bonfà, R. De Renzi, L. Monacelli, F. Mauri, M. Calandra, and I. Errea, Quantum effects in muon spin spectroscopy within the stochastic self-consistent harmonic approximation, [Phys. Rev. Materials](#) **3**, 073804 (2019).
  23. V. G. Storchak and N. V. Prokof'ev, Quantum diffusion of muons and muonium atoms in solids, [Rev. Mod. Phys.](#) **70**, 929 (1998).
  24. C. P. Herrero and R. Ramírez, Diffusion of muonium and hydrogen in diamond, [Phys. Rev. Lett.](#) **99**, 205504 (2007).
  25. B. Huddart, A. Hernández-Melián, T. Hicken, M. Gomilšek, Z. Hawkhead, S. Clark, F. Pratt, and T. Lancaster, Mufinder: A program to determine and analyse muon stopping sites, [Comput. Phys. Commun.](#) **280**, 108488 (2022).
  26. A. V. Soudackov and S. Hammes-Schiffer, Removal of the double adiabatic approximation for proton-coupled electron transfer reactions in solution, [Chem. Phys. Lett.](#) **299**, 503 (1999).
  27. A. R. Porter, M. D. Towler, and R. J. Needs, Muonium as a hydrogen analogue in silicon and germanium: Quantum effects and hyperfine parameters, [Phys. Rev. B](#) **60**, 13534 (1999).
  28. P. Bonfà, F. Sartori, and R. De Renzi, Efficient and reliable strategy for identifying muon sites based on the double adiabatic approximation, [J. Phys. Chem. C](#) **119**, 4278 (2015).
  29. L. Monacelli, R. Bianco, M. Cherubini, M. Calandra, I. Errea, and F. Mauri, The stochastic self-consistent harmonic approximation: calculating vibrational properties of materials with full quantum and anharmonic effects, [J. Phys. Condens. Matter.](#) **33**, 363001 (2021).
  30. M. A. Boxwell, T. A. Claxton, and S. F. J. Cox, *Ab initio* calculations on the hyperfine isotope effect between C<sub>60</sub>H and C<sub>60</sub>Mu, [J. Chem. Soc., Faraday Trans.](#) **89**, 2957 (1993).
  31. J. S. Möller, D. Ceresoli, T. Lancaster, N. Marzari, and S. J. Blundell, Quantum states of muons in fluorides, [Phys. Rev. B](#) **87**, 121108(R) (2013).
  32. K. Yamada, Y. Kawashima, and M. Tachikawa, Accurate prediction of hyperfine coupling constants in muoniated and hydrogenated ethyl radicals: *ab initio* path integral simulation study with density functional theory method, [J. Chem. Theory Comput.](#) **10**, 2005 (2014).
  33. M. B. Plenio and S. Virmani, An introduction to entanglement measures, [Quantum Info. Comput.](#) **7**, 1–51 (2007).
  34. R. Horodecki, P. Horodecki, M. Horodecki, and K. Horodecki, Quantum entanglement, [Rev. Mod. Phys.](#) **81**, 865 (2009).
  35. R. Horodecki, Quantum information, [Acta Phys. Pol.](#) **139**, 197 (2021).
  36. T. A. Claxton, Muon-nuclear quadrupolar level crossing resonance in solid nitrogen. Evidence for [N<sub>2</sub>MuN<sub>2</sub>]<sup>+</sup> complex formation?, [Philos. Mag. B](#) **72**, 251 (1995).
  37. A. Abragam, Spectrométrie par croisements de niveaux en physique du muon, [C. R. Acad. Sci. Ser. B](#) **229**, 95 (1984).
  38. V. Storchak, G. Morris, K. Chow, W. Hardy, J. Brewer, S. Kreitzman, M. Senba, J. Schneider, and P. Mendels, Muon—nuclear quadrupolar level crossing resonance in solid nitrogen. Evidence for N<sub>2</sub>μ<sup>+</sup> ion formation, [Chem. Phys. Lett.](#) **200**, 546 (1992).
  39. J. S. Lord, F. L. Pratt, and M. T. F. Telling, Time differential ALC – experiments, simulations and benefits, [J. Phys. Conf. Ser.](#) **551**, 012058 (2014).
  40. T. A. Scott, Solid and liquid nitrogen, [Phys. Rep.](#) **27**, 89 (1976).
  41. A. Erba, L. Maschio, S. Salustro, and S. Casassa, A post-Hartree–Fock study of pressure-induced phase transitions in solid nitrogen: The case of the  $\alpha$ ,  $\gamma$ , and  $\varepsilon$  low-pressure phases, [J. Chem. Phys.](#) **134**, 074502 (2011).
  42. J. Rumble, [CRC Handbook of Chemistry and Physics](#), 102nd ed. (CRC Press/Taylor & Francis Group, Boca Raton, 2021).
  43. P. Botschwina, T. Dutoi, M. Mladenović, R. Oswald, S. Schmatz, and H. Stoll, Theoretical investigations of proton-bound cluster ions, [Faraday Discuss.](#) **118**, 433 (2001).
  44. K. Terrill and D. J. Nesbitt, *Ab initio* anharmonic vibrational frequency predictions for linear proton-bound complexes OC–H<sup>+</sup>–CO and N<sub>2</sub>–H<sup>+</sup>–N<sub>2</sub>, [Phys. Chem. Chem. Phys.](#) **12**, 8311 (2010).
  45. Q. Yu, J. M. Bowman, R. C. Fortenberry, J. S. Mancini, T. J. Lee, T. D. Crawford, W. Klemperer, and J. S. Francisco, Structure, anharmonic vibrational frequencies, and intensities of NNHNN<sup>+</sup>, [J. Phys. Chem. A](#) **119**, 11623 (2015).
  46. H.-Y. Liao, M. Tsuge, J. A. Tan, J.-L. Kuo, and Y.-P. Lee, Infrared spectra and anharmonic coupling of proton-bound nitrogen dimers N<sub>2</sub>–H<sup>+</sup>–N<sub>2</sub>, N<sub>2</sub>–D<sup>+</sup>–N<sub>2</sub>, and <sup>15</sup>N<sub>2</sub>–H<sup>+</sup>–<sup>15</sup>N<sub>2</sub> in solid para-hydrogen, [Phys. Chem. Chem. Phys.](#) **19**, 20484 (2017).
  47. R. Hooper, D. Boutwell, and M. Kaledin, Assignment of infrared-active combination bands in the vibrational spectra of protonated molecular clusters using driven classical trajectories: Application to N<sub>4</sub>H<sup>+</sup> and N<sub>4</sub>D<sup>+</sup>, [J. Phys. Chem. A](#) **123**, 5613 (2019).
  48. V. Storchak, J. H. Brewer, G. D. Morris, D. J. Arseneau, and M. Senba, Muonium formation via electron transport in solid nitrogen, [Phys. Rev. B](#) **59**, 10559 (1999).
  49. G. P. Srivastava, [The Physics of Phonons](#) (A. Hilger, Bristol Philadelphia, 1990).
  50. L. Kantorovich, [Quantum Theory of the Solid State: An Introduction](#) (Kluwer Academic Publishers, Dordrecht Boston, 2004).
  51. M. Shiga, Path integral simulations, in [Reference Module in Chemistry, Molecular Sciences and Chemical Engineering](#) (Elsevier, 2018).
  52. T. Ichiye and M. Karplus, Collective motions in proteins: A covariance analysis of atomic fluctuations in molecular dynamics and normal mode simulations, [Proteins](#) **11**, 205 (1991).
  53. M. Tokman, D. Sundholm, P. Pyykkö, and J. Olsen, The nuclear quadrupole moment of <sup>14</sup>N obtained from finite-element MCHF calculations on N<sup>2+</sup> (2p; <sup>2</sup>P<sub>3/2</sub>) and N<sup>+</sup> (2p<sup>2</sup>; <sup>3</sup>P<sub>2</sub> and 2p<sup>2</sup>; <sup>1</sup>D<sub>2</sub>), [Chem. Phys. Lett.](#) **265**, 60

- (1997).
54. M. J. W. Hall, D.-A. Deckert, and H. M. Wiseman, Quantum phenomena modeled by interactions between many classical worlds, *Phys. Rev. X* **4**, 041013 (2014).
  55. S. Sturmiolo, Computational applications of the many-interacting-worlds interpretation of quantum mechanics, *Phys. Rev. E* **97**, 053311 (2018).
  56. I. Errea, M. Calandra, C. J. Pickard, J. Nelson, R. J. Needs, Y. Li, H. Liu, Y. Zhang, Y. Ma, and F. Mauri, High-pressure hydrogen sulfide from first principles: A strongly anharmonic phonon-mediated superconductor, *Phys. Rev. Lett.* **114**, 157004 (2015).
  57. I. Errea, M. Calandra, C. J. Pickard, J. R. Nelson, R. J. Needs, Y. Li, H. Liu, Y. Zhang, Y. Ma, and F. Mauri, Quantum hydrogen-bond symmetrization in the superconducting hydrogen sulfide system, *Nature* **532**, 81 (2016).
  58. M. Somayazulu, M. Ahart, A. K. Mishra, Z. M. Geballe, M. Baldini, Y. Meng, V. V. Struzhkin, and R. J. Hemley, Evidence for superconductivity above 260 K in lanthanum superhydride at megabar pressures, *Phys. Rev. Lett.* **122**, 027001 (2019).
  59. I. Errea, F. Belli, L. Monacelli, A. Sanna, T. Koretsune, T. Tadano, R. Bianco, M. Calandra, R. Arita, F. Mauri, *et al.*, Quantum crystal structure in the 250-kelvin superconducting lanthanum hydride, *Nature* **578**, 66 (2020).
  60. J. Hirsch and F. Marsiglio, Unusual width of the superconducting transition in a hydride, *Nature* **596**, E9 (2021).
  61. S. J. Clark, M. D. Segall, C. J. Pickard, P. J. Hasnip, M. J. Probert, K. Refson, and M. Payne, First principles methods using CASTEP, *Z. Kristall.* **220**, 567 (2005).
  62. J. P. Perdew, K. Burke, and M. Ernzerhof, Generalized gradient approximation made simple, *Phys. Rev. Lett.* **77**, 3865 (1996).
  63. H. J. Monkhorst and J. D. Pack, Special points for Brillouin-zone integrations, *Phys. Rev. B* **13**, 5188 (1976).
  64. A. Tkatchenko and M. Scheffler, Accurate molecular Van Der Waals interactions from ground-state electron density and free-atom reference data, *Phys. Rev. Lett.* **102**, 073005 (2009).
  65. H. E. Maynard-Casely, J. R. Hester, and H. E. A. Brand, Re-examining the crystal structure behaviour of nitrogen and methane, *IUCrJ* **7**, 844 (2020).
  66. S. E. Ashbrook and M. J. Duer, Structural information from quadrupolar nuclei in solid state NMR, *Concepts Magn. Reson. Part A Bridg. Educ. Res.* **28A**, 183 (2006).
  67. C. Slichter, *Principles of Magnetic Resonance* (Springer, Berlin, 1990).
  68. F. L. Pratt, A User Tool for Predicting and Interpreting Muon ALC and QLCR Spectra, <http://shadow.nd.rl.ac.uk/calcalc/>, accessed: 2021-09-17.
  69. A. Berlie, F. L. Pratt, B. M. Huddart, T. Lancaster, and S. P. Cottrell, Muon–nitrogen quadrupolar level crossing resonance in a charge transfer salt, *J. Phys. Chem. C* **126**, 7529 (2022).
  70. J. Lord, S. Cottrell, and W. Williams, Muon spin relaxation in strongly coupled systems, *Physica B Condens. Matter* **289-290**, 495 (2000).
  71. P. Zyla *et al.* (Particle Data Group), Review of Particle Physics, *Prog. Theor. Exp. Phys.* **2020**, 10.1093/ptep/ptaa104 (2020), 083C01, <https://academic.oup.com/ptep/article-pdf/2020/8/083C01/34673722/ptaa104.pdf>.
  72. S. Giblin, S. Cottrell, P. King, S. Tomlinson, S. Jago, L. Randall, M. Roberts, J. Norris, S. Howarth, Q. Muntamba, N. Rhodes, and F. Akeroyd, Optimising a muon spectrometer for measurements at the ISIS pulsed muon source, *Nucl. Instrum. Methods Phys. Res. A* **751**, 70 (2014).
  73. Data and computer code from this paper can be found at <https://dx.doi.org/10.6084/m9.figshare.23203037>.

#### ACKNOWLEDGMENTS

The authors acknowledge helpful discussions with A. Zorko. Part of this work was performed at the STFC-ISIS facility. Computing resources were provided by the STFC Scientific Computing Department’s SCARF cluster and the Durham HPC Hamilton cluster. M.G., T.L., S.J.C., and F.L.P. are grateful to Engineering and Physical Sciences Research Council (EPSRC, UK) for financial support through Grants No. EP/N024028/1 and EP/N024486/1. M.G. is grateful to the Slovenian Research Agency (ARRS) for financial support through Projects No. Z1-1852 and J1-2461 and Programme No. P1-0125.

#### AUTHOR CONTRIBUTIONS

The project was originally conceived by T.L. and F.L.P. M.G. carried out DFT, MD, and PIMD calculations under the supervision of T.L. and S.J.C., and developed the unified description of muon–nuclear entanglement and anharmonicity. F.L.P. and S.P.C. conceived of and set up the QLCR experiments and performed them with assistance from M.G. QLCR data was analyzed by F.L.P., S.P.C., and M.G. with QLCR calculations performed by M.G. and F.L.P. All authors discussed the results. M.G. wrote the paper with feedback from all the authors.

#### COMPETING INTERESTS

The authors declare no competing interests.

#### ADDITIONAL INFORMATION

Correspondence and requests for materials should be addressed to M.G.

# Supplementary Information: Many-Body Quantum Muon Effects and Quadrupolar Coupling in Solids

Matjaž Gomilšek <sup>1,2,3,\*</sup> Francis L. Pratt <sup>4</sup> Stephen P. Cottrell <sup>4</sup> Stewart J. Clark <sup>3</sup> and Tom Lancaster <sup>3</sup>

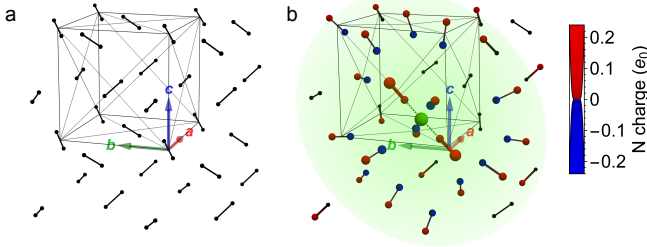
<sup>1</sup>Jožef Stefan Institute, Jamova c. 39, SI-1000 Ljubljana, Slovenia

<sup>2</sup>Faculty of Mathematics and Physics, University of Ljubljana, Jadranska u. 19, SI-1000 Ljubljana, Slovenia

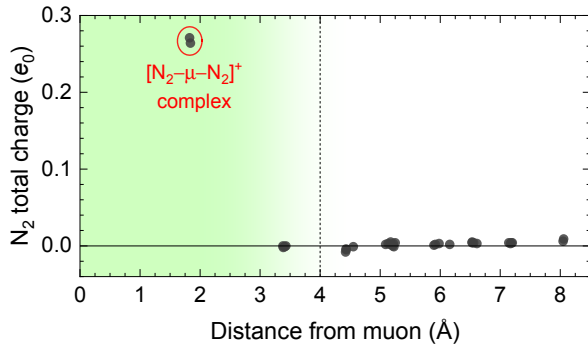
<sup>3</sup>Department of Physics, Durham University, South Road, Durham DH1 3LE, United Kingdom

<sup>4</sup>ISIS Muon Group, Science and Technology Facilities Council (STFC), Didcot OX11 0QX, United Kingdom

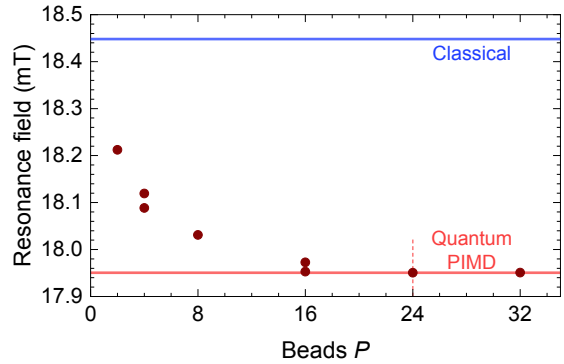
(Dated: June 22, 2023)



**Supplementary Fig. 1. Pristine and muonated crystal structures of solid nitrogen,  $\alpha$ -N<sub>2</sub>.** Alternative views of **a** the pristine  $\alpha$ -N<sub>2</sub> structure, where the centers of N<sub>2</sub> molecules form a face-centered cubic lattice (gray lines), and **b** the classical muon site, where  $\mu^+$  (green) forms a linear  $[\text{N}_2-\mu-\text{N}_2]^+$  complex with the two neighboring N<sub>2</sub> molecules at the center of an electric-dipole polaron (shading) [cf. Fig. 1a, b in the main text]. Induced Mulliken charge of nitrogen ions from density functional theory (DFT) calculations is represented by sphere size and color.

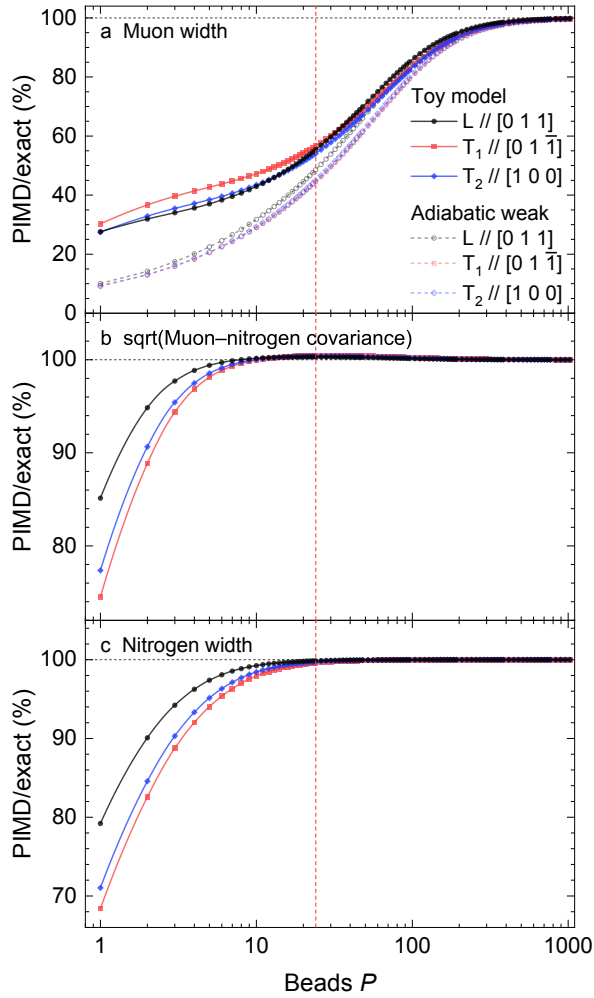


**Supplementary Fig. 2. Electric charge of N<sub>2</sub> molecules in muonated  $\alpha$ -N<sub>2</sub>.** Net Mulliken electric charge on N<sub>2</sub> molecules in muonated  $\alpha$ -N<sub>2</sub> for a classical muon site (see also Fig. 1b in the main text, [Supplementary Fig. 1b](#), and [Supplementary Movie 2](#)) from DFT. The only excess of net charge is seen within the  $[\text{N}_2-\mu-\text{N}_2]^+$  complex due to polar covalent bonding of the two N<sub>2</sub> molecules with  $\mu^+$ , which leaves them slightly positively charged while the muon's positive charge gets partially screened by negatively-charged electrons shared with the two N<sub>2</sub>.

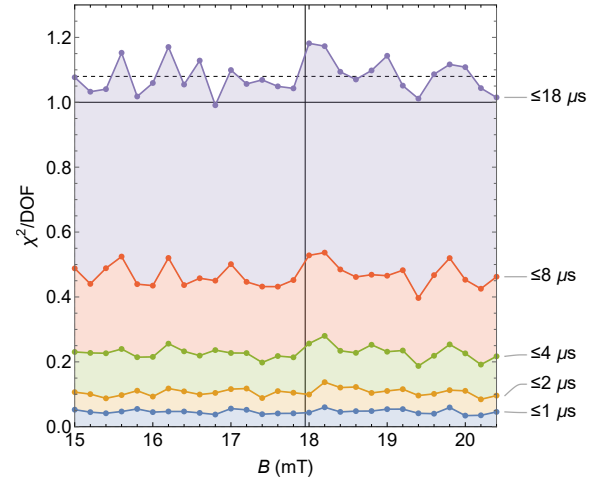


**Supplementary Fig. 3. Path-integral molecular dynamics (PIMD) convergence.** Convergence of PIMD calculations with the number of beads  $P$  as observed from the calibrated quadrupolar level-crossing resonance (QLCR) peak resonance field from a muon-lifetime weighed integral of the QLCR signal over a 4–8  $\mu\text{s}$  time window. The final number of beads  $P = 24$  for PIMD calculations presented in the main text is indicated by the dashed line.

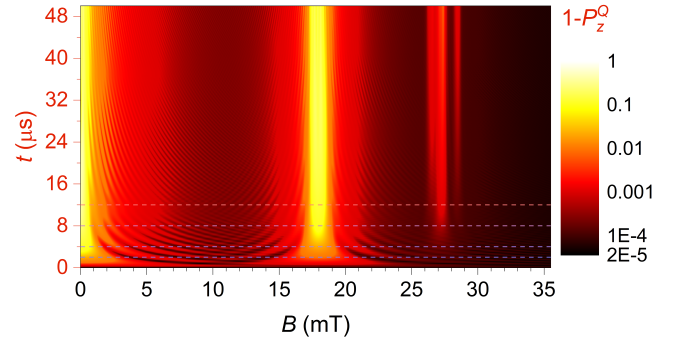
\* Corresponding author. Email: [matjaz.gomilsek@ijs.si](mailto:matjaz.gomilsek@ijs.si)



**Supplementary Fig. 4. Predicted PIMD convergence in the harmonic approximation.** Predicted convergence of PIMD calculations with the number of beads  $P$  as observed from: **a** the muon wavefunction widths  $\Delta x_j$ , **b** the covariances of muon and nitrogen positions, and **c** the nitrogen wavefunction widths along the  $j = L, T_1$ , and  $T_2$  directions. Solid lines are predictions of the toy model with  $N = 2$  nearest nuclei described in the main text, while dashed lines represent predictions under the harmonic weakly-bound adiabatic approximation, i.e., for a single muon in an effective harmonic potential of Fig. 2a,b. The final number of beads  $P = 24$  for PIMD calculations is indicated by the vertical dashed line.



**Supplementary Fig. 5. Quality of QLCR spectra fits.** Field- and time-resolved quality of the global fits of experimental QLCR spectra using PIMD at  $T = 5$  K as described in the main text. The contributions towards the total reduced  $\chi^2/\text{DOF}$  at each applied field  $B$  are shown cumulatively up to different times after muon implantation. The horizontal dashed line shows the average  $\chi^2/\text{DOF} = 1.08$  across all  $B$  (i.e., the total  $\chi^2/\text{DOF}$  of the global fit), while the vertical line shows the main QLCR resonance field (Supplementary Fig. 3).



**Supplementary Fig. 6. Time-dependent PIMD QLCR spectra.** Calibrated QLCR spectra,  $1 - P_z^Q$ , from PIMD calculations with 24 beads for time-differential QLCR analysis. Dashed lines indicate time window boundaries for QLCR signal integrals shown in Fig. 3b in the main text.